Effect of loading history on airway smooth muscle cell–matrix adhesions

Linda Irons, Markus R. Owen, Reuben D. O'Dea, Bindi S. Brook

Centre for Mathematical Medicine and Biology, School of Mathematical Sciences
University of Nottingham, Nottingham, NG7 2RD, UK

Abstract

Integrin-mediated adhesions between airway smooth muscle (ASM) cells and the extracellular matrix (ECM) regulate how contractile forces generated within the cell are transmitted to its external environment. Environmental cues are known to influence the formation, size and survival of cell–matrix adhesions, but it is not yet known how they are affected by dynamic fluctuations associated with tidal breathing in the intact airway. Here we develop two closely-related theoretical models to study adhesion dynamics in response to oscillatory loading of the ECM, representing the dynamic environment of ASM cells *in vivo*. Using a discrete stochastic-elastic model, we simulate individual integrin binding and rupture events and observe two stable regimes in which either bond formation or bond rupture dominate, depending on the amplitude of the oscillatory loading. These regimes have either a high or low fraction of persistent adhesions, which could affect the level of strain transmission between contracted ASM cells and the airway tissue. For intermediate loading we observe a region of bistability and hysteresis due to shared loading between existing bonds; the level of adhesion depends on the loading history. These findings are replicated in a related continuum model, which we use to investigate the effect of perturbations mimicking deep inspirations (DIs). Due to the bistability, a DI applied to the high adhesion state could either induce a permanent switch to a lower adhesion state or allow a return of the system to the high adhesion state. Transitions between states are further influenced by the frequency of oscillations, cytoskeletal or ECM stiffnesses and binding affinities, which modify the magnitudes of the stable adhesion states as well as the region of bistability. These findings could explain (in part) the transient bronchodilatory effect of a DI observed in asthmatics compared to a more sustained effect in normal subjects.

1 Introduction

Contraction of airway smooth muscle (ASM) cells is typically triggered by exposure to irritants or allergens and leads to bronchoconstriction, a narrowing of the airways characteristic of asthma (1). Contracted ASM cells transmit strain to the extracellular matrix (ECM), and hence the airways, via focal adhesions (2, 3), of which integrins are a key component. Integrins are transmembrane proteins that provide the necessary mechanical link between the intracellular and extracellular domains by binding to the cytoskeletal network within the cell and to ligands in the ECM (4, 5). Since it is well-established that integrins are responsive to mechanical and environmental cues (6–8) we expect the environment of the *in vivo* airway, which is inherently dynamic due to tidal breathing, to modulate the integrin binding dynamics and consequent levels of strain transmission. Several experimental studies have shown that tidal breathing and deep inspirations (DIs) are able to modulate the levels of contractile force in healthy airways (9–11). In particular, DIs are capable of inducing bronchodilation (reversing airway narrowing) in healthy subjects but these effects are either transient or diminished in asthmatics. To understand this, a number of studies at the cell-level and tissue-level have focussed on the ASM cell response to oscillatory loading and consequent modulation of contractile force generation (12–15). Disruption of actin-myosin crossbridge cycling, which mediates contractile force generation within the cell, reduces the mean contractile force. However, the role of cell–matrix adhesions in understanding how the strain due to contraction is transmitted to the tissue could also be an important factor, and has so far been neglected.

To enable strain transmission between the cell and the ECM, a sequence of molecular events takes place

that connect integrins to both the intracellular and extracellular regions of the cell. These events can be thought of as reversible state transitions, where integrins belong to one of five states (depicted in Fig. 1). Inactive integrins freely diffuse in the plasma membrane in a bent conformation that leaves them close to the membrane and with a low affinity for binding to ligands in the ECM. Integrin activation occurs in stages, with a final stage being recognised as the binding of adaptor proteins—commonly talin—to the integrin cytoplasmic tail (16, 17). At this stage, the active integrin extends into an upright conformation where it is more readily available for ligand binding. The adaptor proteins additionally form the link to the actin cytoskeleton. Once bound to both the actin cytoskeleton and to ligands in the ECM, the integrins form a physical link between intracellular and extracellular domains, enabling transmission of mechanical strain.
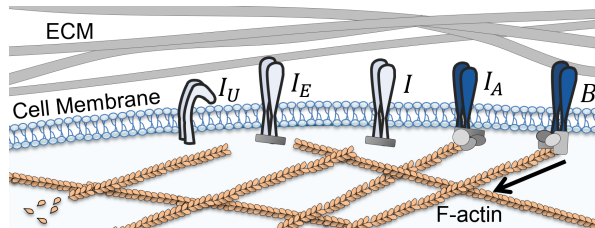

Figure 1: Representation of the five possible integrin states. Inactive (I_U) and active (I) integrins diffuse in the membrane. Active integrins may become actin-bound (I_A) via adaptor proteins, bound to ligands in the ECM (I_E) or double-bound to both the actin cytoskeleton and the ECM (B). In our models, we consider actin-bound and double-bound integrins (blue).

In previous models the binding dynamics of individual integrin–ligand bonds have been studied using stochastic simulations. A number of studies (18–20) investigate the stochastic rupture of parallel bonds under shared loading, and Qian *et al.* (21) extend this by considering bonds that experience stress non-uniformly due to an inclined loading angle. Of particular relevance to the current work are studies that consider the effect of dynamic loading on adhesion stability (22), measured by the mean change in number of bound integrins when subject to the external load. Kong *et al.* (22) consider the rupture of adhesion clusters under an oscillatory strain and, starting from a high adhesion state, a threshold strain is observed past which adhesions quickly rupture. In a related modelling framework, although not concerned with external loading, Paszek *et al.* (23) use lattice spring models together with a stochastic simulation algorithm for modelling integrin–ligand bonds, called Adhesive Dynamics (24, 25), to simulate the formation of integrin clusters. Stochastic models are a common approach for studying the mechanosensitive nature of cell–matrix adhesion. Chan and Odde (26) and Walcott *et al.* (27) both use stochastic models to investigate the differing adhesion dynamics on stiff and compliant ECM, and obtain results in agreement with experimental studies. Walcott *et al.* (27) show that mechanosensitive adhesion properties emerge naturally with the inclusion of load dependent reactions.

Studies considering friction generated by discrete bonds in more general contexts are also relevant to modelling cell–matrix adhesions. Filippov *et al.* (28) consider the stochastic formation and rupture of discrete molecular bonds between two rigid surfaces and simulate macroscopic friction properties with high and low relative velocities of the surfaces. In a closely related study, Srinivasan and Walcott (29) develop a continuum approximation through the use of the Lacker-Peskin model (30), and find that well-known steady slip and stick-slip friction behaviours are captured. Given the potentially large number of integrins present on the cell surface (densities have been reported to reach $900\mu\mathrm{m}^{-2}$ in mature adhesions (31)), stochastic models can become prohibitive; continuum models therefore have greater utility in such cases, allowing for a more comprehensive exploration of the system behaviour. Welf *et al.* (32) and Block *et al.* (33) have developed continuum models for integrin binding and for integrin clustering based on biochemical feedback in reaction-diffusion systems. However, these studies do not accommodate the response to local mechanical cues. Integrins are highly mechanosensitive, and Cao *et al.* (34, 35) have developed continuum models that allow for investigation of the effect of substrate and cell nucleus stiffness on focal adhesion size. The timescale of interest in their studies (focal adhesion growth, occuring over minutes) is relatively large compared to the timescale associated with individual integrin binding reactions, so a quasi-static approximation for the density of integrins is used. A full review of existing models is not presented here, but other note-

worthy examples of models that capture experimentally observed focal adhesion behaviour include (36–38). Further examples of stochastic models have been reviewed by Gao *et al.* (39).

In this paper, we develop two closely-related theoretical models to investigate integrin binding and adhesion dynamics between an ASM cell and the surrounding ECM in a dynamic environment. Firstly we consider a discrete stochastic-elastic model for cell–matrix adhesion, and investigate how tidal breathing influences the formation and survival of adhesions. We then develop an analogous multiscale continuum model that couples microscale binding reactions to the mechanical environment, and reproduces the qualitative behaviour observed in the stochastic simulations. With the more tractable continuum model we further investigate how material parameters and deep inspirations may affect the adhesion properties of ASM cells *in vivo*.

2 Methods

In the models that follow we consider a simplified reaction scheme where the previously described integrin activation processes are assumed to have already occurred. We therefore assume that integrins are already attached to the actin cytoskeleton within the cell and undergo reversible reactions to become bound to the ECM and able to transmit force (I_A binds reversibly to B, see Fig. 1). Similarly to Paszek *et al.* (23), in our discrete model we represent the cell, ECM and bound integrins by a network of linear springs, but focus on the effect of dynamic loading by introducing an oscillatory shear displacement of the ECM. In our continuum model we capture microscale binding reactions at the integrin level using an adaptation of the Lacker-Peskin model (30); these integrin dynamics respond to (and generate) ECM and cell deformations at the cell level. Through this multiscale approach, we are able to account for microscale spatial constraints in the binding and unbinding reactions in a similar manner to the individual-based approach used in the discrete model.

2.1 Discrete model formulation

The discrete model comprises an evolving network of nodes and linear springs, the structure of which is governed by stochastic reactions representing transitions between the integrin states I_A and B, described above. By modelling individual interactions between integrins, the cell and the ECM, we aim first to develop an intuitive understanding of cell–matrix adhesion. We assume that the cytoskeleton, integrins and ECM form a spring network in which actin-bound integrins (I_A) and 'potential binding sites' on the ECM fibre (E) are modelled as individual nodes, indexed by I_{A_j} and E_i, respectively (Fig. 2). Hookean springs between the neighbouring I_A and E nodes represent the cytoskeleton and ECM, respectively, and are each assigned a spring stiffness (κ_a and κ_e). Reactions between integrins and the ECM are dependent on the proximity and availability of binding sites, and each node is considered to be an individual species so that reaction propensities depend on their pairwise distances. Pairs of compatible nodes may undergo stochastic transitions to form fully-bound integrins (B) according to the following reaction

$$I_A + E \underset{\hat{k}_u(\hat{x})}{\overset{\hat{k}_b(\hat{x})}{\rightleftharpoons}} B, \tag{1}$$

where $\hat{x}$ is a spatial variable local to each integrin that, following (40), measures the horizontal distance between each pair of I_A and E nodes (see Fig. 2) and is therefore effectively a measure of how far each integrin head is from its unstressed position, $\hat{x} = 0$. Throughout, hats indicate dimensional quantities. In accordance with these stochastic reactions we add or remove a third spring-type (representing double-bound integrins with stiffness κ_b) between the I_A and E nodes selected to bind. We additionally include springs with stiffness κ_r from the I_A nodes to a fixed configuration of 'anchor' nodes, as a representation of the restoring forces and attachments to the cytoskeletal network within the cell. Following (40), the vertical movement is constrained and we only consider horizontal motion, a physical simplification which will be addressed in future work (see Discussion).

We select the reversible binding events using a stochastic first reaction algorithm (41) and follow the reactions
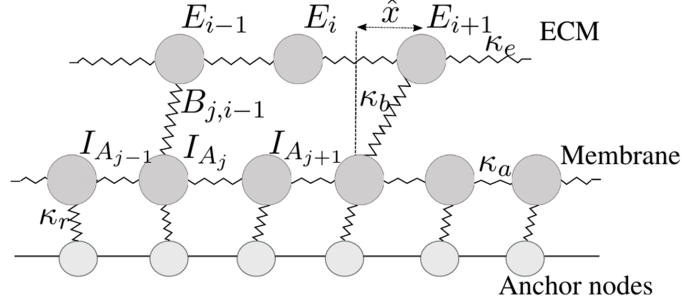
Figure 2: Structure of the discrete spring network. Following (40), the vertical movement is constrained and we only consider horizontal motion. Actin-bound integrins (I_A) and ECM binding sites (E) are considered as individual nodes, connected to their neighbours by linear springs with stiffness constants κ_a and κ_e respectively. Bound integrins (B) are represented by removable springs between the two sets of nodes, with spring constant κ_b. The local variable $\hat{x}$ measures horizontal distances between pairs of integrin and ECM binding site nodes. We additionally include horizontal restoring forces for the I_A nodes to a fixed configuration of anchor nodes via springs with stiffness κ_r.

in Eq. 1 for each pair of compatible nodes. In this work our chosen spatial binding rates are piecewise linear functions (Fig. 3) given by

$$
\hat{k}_b(\hat{x}) = \begin{cases} \hat{f}_1 \left(1 - \frac{|\hat{x}|}{\hat{h}}\right) & |\hat{x}| \leq \hat{h}, \\ 0 & \text{otherwise}, \end{cases} \tag{2}
$$

and

$$
\hat{k}_u(\hat{x}) = \begin{cases} \hat{g}_1 + \frac{\hat{g}_2 |\hat{x}|}{\hat{h}} & |\hat{x}| \leq \hat{s}, \\ \hat{g}_3 & \text{otherwise}. \end{cases} \tag{3}
$$

A maximum binding rate $\hat{f}_1$ occurs at $\hat{x} = 0$, after which the binding propensity decreases linearly to zero within a finite binding range, $\hat{h}$. The unbinding rate when $\hat{x} = 0$ is given by $\hat{g}_1$, and increases at a rate $\hat{g}_2/\hat{h}$ as $\hat{x}$ increases. Beyond a maximum horizontal distance of $\hat{s}$, any remaining bonds rupture quickly with a high rate $\hat{g}_3$. We note that these piecewise linear rates approximate those which can be derived using detailed balance (see e.g. (42), Fig. 9c and (29), Fig. 2), by which pairs of reaction rates are constrained to ensure thermodynamic reversibility. Within this modelling framework there is flexibility in the choice of rate functions, and alternative choices can be used (see Discussion).
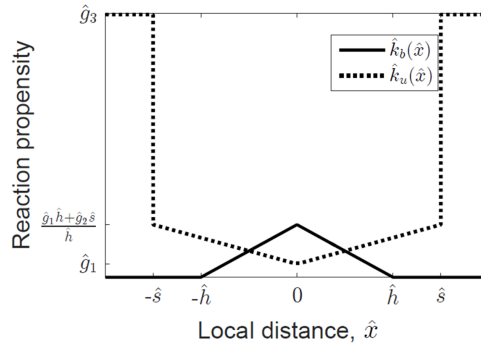

Figure 3: Sketch of the chosen form of piecewise linear binding ($\hat{k}_b$, Eq. 2) and unbinding ($\hat{k}_u$, Eq. 3) functions. The local variable $\hat{x}$ measures the local distance between pairs of ECM and actin-bound integrin nodes (see Fig. 2) and is therefore effectively a measure of how far each integrin head is from its unstressed position, $\hat{x} = 0$.

The stochastic reactions that govern bond formation and rupture are used to update the structure of the mechanical spring network (Fig. 2). To implement a position update of the network we consider the net force acting on each node, $\hat{F}_k$. There are contributions due to neighbouring springs, $\hat{F}_{N_k}$, and forces due to integrin bonds between species, $\hat{F}_{B_k}$. In this model, electrostatic interactions and inertia are assumed to be

4

negligible. We therefore take $\hat{\boldsymbol{F}}_k = \hat{\boldsymbol{F}}_{N_k} + \hat{\boldsymbol{F}}_{B_k}$ and update the positions of the nodes to ensure that $\Sigma\hat{\boldsymbol{F}}_k = \boldsymbol{0}$ at each timestep.

In order to represent fluctuations that occur due to tidal breathing we impose an external, oscillatory, forcing to the ECM via a time-dependent displacement of the boundary node

$$\hat{U}_{E_1}(\hat{t}) = \hat{A}\sin(\hat{\omega}\hat{t}), \tag{4}$$

with amplitude $\hat{A}$, frequency $\frac{\hat{\omega}}{2\pi}$, and where $\hat{U}_{E_i}$ denotes the displacement of the ith ECM node from its rest position. Sinusoidal waveforms are commonly used to represent tidal breathing (43–46); however, they are a simplification since exhalation is typically longer than inhalation. We include and discuss results for an asymmetric waveform in Section S.3.2 in the Supporting Material. The results and conclusions are consistent with those presented here.

We note that the first reaction algorithm (41) generates an event-based timestep. As we are also considering external forcing we introduce a maximum timestep $\hat{\tau}_{max}$ such that, in the case that no reaction occurs within this timestep, a position update of the network is induced and reaction propensities are recalculated. We summarise the computational model in Section S.1.1 in the Supporting Material.

2.2 Continuum model formulation

We now introduce an analogous continuum model in which we consider two well-separated scales: a microscale integrin-level description for bond formation and rupture, that is coupled to a macroscale cell-level model of material deformation (illustrated in Fig. 4). At the macroscale, we consider deformations of the cell, $\hat{U}_A(\hat{X}, \hat{t})$, and of the ECM, $\hat{U}_E(\hat{X}, \hat{t})$, where $\hat{X}$ is a macroscale spatial coordinate and $\hat{t}$ is time. At each point in $\hat{X}$ a macroscale deformation occurs as a result of the adhesive drag force, $\hat{F}(\hat{X}, \hat{t})$, which is generated by integrins cycling between bound and unbound states at the microscale. To model the microscale reactions we adapt an existing model by Lacker and Peskin (30) (an extension of the Huxley model (40) for actin-myosin crossbridge dynamics, discussed in detail in (29)).
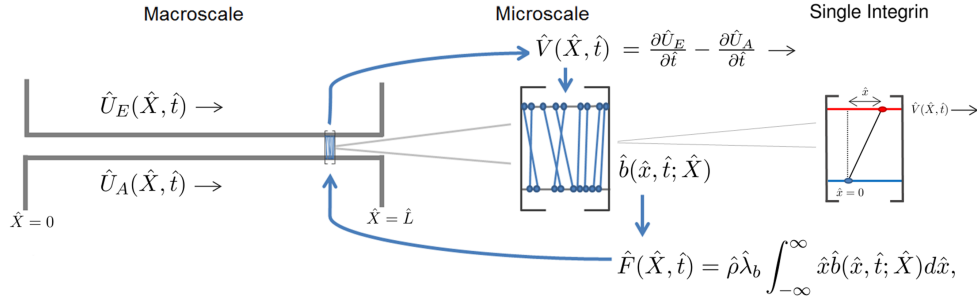

Figure 4: Schematic diagram of the multiscale coupling. A relative velocity $\hat{V}(\hat{X}, \hat{t})$, arising from macroscale deformation, influences the binding dynamics and distribution of bonds, $\hat{b}(\hat{x}, \hat{t}; \hat{X})$ in a corresponding microscale problem (Eq. 6). As in the discrete model, the variable $\hat{x}$ is local to each integrin and measures the horizontal distance from the cytoskeletal attachment to the binding site on the ECM, as shown. Microscale distributions determine the horizontal drag force, $\hat{F}(\hat{X}, \hat{t})$, which is used to update the displacements $\hat{U}_A$ and $\hat{U}_E$ and thereby $\hat{V}(\hat{X}, \hat{t})$ (via Eqs. 7–9).

2.2.1 Microscale governing equations

At the microscale we again consider the binding of active, actin-bound integrins (I_A) to the ECM to form double-bound integrins (B, Eq. 1). Following the Lacker-Peskin model, the ECM binding sites are assumed to be densely distributed, and there is a characteristic length scale, $\hat{l}$, associated with the spacing between sites. Each double-bound integrin is associated with a local variable, $\hat{x}$, measuring the horizontal distance of the bound integrin head from its unstressed (vertical) position at $\hat{x} = 0$. In the unstressed position, the integrin does not contribute to the horizontal drag force. At each point in the macroscale domain, $\hat{X} \in$

$\left[0, \hat{L}\right]$, bound integrins are collectively expressed by a distribution, $\hat{b}(\hat{x}, \hat{t}; \hat{X})$, such that the fraction of integrins that are bound with local displacements in a range of $[\hat{x}, \hat{x} + \Delta\hat{x}]$ at time $\hat{t}$ is given by the integral $\int_{\hat{x}}^{\hat{x}+\Delta\hat{x}} \hat{b}(\hat{x}, \hat{t}; \hat{X})d\hat{x}$. The total fraction of bound integrins is given by

$$B(\hat{X}, \hat{t}) = \int_{-\infty}^{\infty} \hat{b}(\hat{x}, \hat{t}; \hat{X})d\hat{x}. \tag{5}$$

The evolution of each microscale distribution is governed by the advection–reaction equation

$$\frac{\partial \hat{b}}{\partial \hat{t}} + \hat{V}\frac{\partial \hat{b}}{\partial \hat{x}} = \frac{\hat{k}_b(\hat{x})}{\hat{l}}(1 - B) - \hat{k}_u(\hat{x})\hat{b}, \tag{6}$$

where the functional dependencies have been suppressed for brevity. The right hand side describes binding and unbinding of integrins through the functions $\hat{k}_b(\hat{x})$ and $\hat{k}_u(\hat{x})$ respectively, for which we employ the same rates as in the discrete model (Eqs. 2, 3). The scaling of the binding rate by $\hat{l}$ arises in the derivation of the Lacker-Peskin model, discussed in detail in (29). Distributions are additionally advected with a macroscale velocity, $\hat{V}(\hat{X}, \hat{t})$, which is the velocity of the ECM relative to the velocity of the cell. By treating integrins as Hookean springs, we obtain the drag force per unit length as

$$\hat{F}(\hat{X}, \hat{t}) = \hat{\rho}\hat{\lambda}_b \int_{-\infty}^{\infty} \hat{x}\hat{b}(\hat{x}, \hat{t}; \hat{X})d\hat{x}, \tag{7}$$

where $\hat{\lambda}_b$ is the integrin spring constant and $\hat{\rho}$ is the number of integrins per unit length, acting at a macroscale point $\hat{X}$. We implicitly assume that there is sufficient scale separation to approximate the microscale distributions to be acting at a macroscale point; a rigorous derivation will be considered in future work.

2.2.2 Macroscale governing equations

At the macroscale we assume that the ECM and cell are linear elastic materials which undergo small deformations. The relative macroscale velocity can be written as

$$\hat{V}(\hat{X}, \hat{t}) = \frac{\partial \hat{U}_E(\hat{X}, \hat{t})}{\partial \hat{t}} - \frac{\partial \hat{U}_A(\hat{X}, \hat{t})}{\partial \hat{t}}, \tag{8}$$

which is coupled to the microscale distributions of bound integrins (see Fig. 4) via Eq. 6.

We assume that the drag forces, $\hat{F}(\hat{X}, \hat{t})$, due to bound integrins are the only body forces acting on the two materials, and hence obtain the following macroscale description by considering quasi-static equilibrium conditions

$$\frac{\partial^2 \hat{U}_A}{\partial \hat{X}^2} = -\frac{1}{\hat{K}_A}\hat{F}, \qquad \frac{\partial^2 \hat{U}_E}{\partial \hat{X}^2} = \frac{1}{\hat{K}_E}\hat{F}. \tag{9}$$

The constants $\hat{K}_A$ and $\hat{K}_E$ are stiffness-like parameters for the cell and ECM, respectively, with units of force per unit strain. The cell and the ECM experience the force in opposite directions.

2.2.3 Boundary Conditions

The cell displacement is assumed to be zero at $\hat{X} = 0$ and $\hat{X} = \hat{L}$ so that

$$\hat{U}_A(0, \hat{t}) = 0, \qquad \hat{U}_A(\hat{L}, \hat{t}) = 0. \tag{10}$$

We apply a time-dependent displacement to the ECM at $\hat{X} = 0$ and zero strain at $\hat{X} = \hat{L}$

$$\hat{U}_E(0, \hat{t}) = \hat{A}\sin(\hat{\omega}\hat{t}), \qquad \frac{\partial \hat{U}_E(\hat{L}, \hat{t})}{\partial \hat{X}} = 0, \tag{11}$$

where the oscillatory displacement is chosen to match the discrete model (Eq. 4).

6

2.2.4 Nondimensionalisation

The governing equations and boundary conditions are nondimensionalised with the scalings

$$x = \hat{x}/\hat{h}, \quad t = \hat{f}_1\hat{t}, \quad U_A = \hat{U}_A/\hat{L}, \quad U_E = \hat{U}_E/\hat{L},$$

$$b = \hat{b}\hat{h}, \quad X = \hat{X}/\hat{L}, \quad V = \hat{V}/\hat{f}_1\hat{L}, \quad F = \hat{F}/\hat{\rho}\hat{h}\hat{\lambda}_b, \tag{12}$$

where $\hat{f}_1$ is the maximum binding rate and $\hat{h}$ is the integrin binding range. For simplicity we assume that $\hat{\rho}$ is uniform, but an extension to non-uniform $\hat{\rho}(\hat{X})$ is easily incorporated. The dimensionless microscale governing equations are

$$\frac{\partial b}{\partial t} + \frac{V}{\delta}\frac{\partial b}{\partial x} = \eta k_b(x)\left(1 - \int_{-\infty}^{\infty} b dx\right) - k_u(x)b, \tag{13}$$

where the dimensionless parameters $\delta = \hat{h}/\hat{L}$ and $\eta = \hat{h}/\hat{l}$ are the ratios of the integrin binding range to the macroscale length scale and to the microscale binding site separation, respectively. The microscale advection–reaction equations are coupled to the macroscale equations via the macroscale velocity $V(X, t)$.

The dimensionless binding rate functions are

$$k_b(x) = \begin{cases} 1 - |x| & |x| \leq 1, \\ 0 & \text{otherwise,} \end{cases} \tag{14}$$

and

$$k_u(x) = \begin{cases} h_1 + h_2|x| & |x| \leq s, \\ h_3 & \text{otherwise,} \end{cases} \tag{15}$$

where $h_i = \hat{g}_i/\hat{f}_1$ are the ratios of unbinding rates to the maximum binding rate, and $s = \hat{s}/\hat{h}$. The dimensionless drag force

$$F(X, t) = \int_{-\infty}^{\infty} x b(x, t; X) dx, \tag{16}$$

features at the macroscale, where the dimensionless governing equations become

$$\frac{\partial^2 U_A}{\partial X^2} = -\frac{1}{K_A}F, \quad \frac{\partial^2 U_E}{\partial X^2} = \frac{1}{K_E}F, \tag{17}$$

with boundary conditions

$$U_A(0, t) = 0, \quad U_A(1, t) = 0,$$

$$U_E(0, t) = A\sin(\omega t), \quad \frac{\partial U_E(1, t)}{\partial X} = 0. \tag{18}$$

The remaining dimensionless parameters are

$$K_A = \hat{K}_A/\hat{\rho}\hat{h}\hat{\lambda}_b\hat{L}, \quad K_E = \hat{K}_E/\hat{\rho}\hat{h}\hat{\lambda}_b\hat{L},$$

$$A = \hat{A}/\hat{L}, \quad \omega = \hat{\omega}/\hat{f}_1. \tag{19}$$

2.2.5 Implementation

To solve the advection–reaction system (Eq. 13), we differentiate the macroscale governing equations (Eq. 17) with respect to time and use Eq. 8 and Eq. 16 to obtain the following second order PDE for $V(X, t)$

$$\frac{\partial^2 V}{\partial X^2} = \gamma H + \frac{\gamma}{\delta}VB, \tag{20}$$

where

$$H = \int_{-\infty}^{\infty} x f(b) \, dx, \quad B = \int_{-\infty}^{\infty} b \, dx, \quad \gamma = \left(\frac{1}{K_E} + \frac{1}{K_A}\right), \tag{21}$$

and

$$f(b) = \eta k_b(x)\,(1 - B) - k_u(x)b. \tag{22}$$

Eqs. 13 and 20 are solved numerically, as detailed in Section S.1.2 in the Supporting Material, subject to

$$V(0,t) = A\omega\cos(\omega t), \qquad \frac{\partial V}{\partial X}(1,t) = 0. \tag{23}$$

The macroscale governing equations (Eq. 17) can be integrated directly to obtain $U_A(X,t)$ and $U_E(X,t)$ in terms of $F(X,t)$. Using Eq. 18, the cell deformation is given by

$$U_A = -\frac{1}{K_A}\int_0^X\int_0^\zeta F d\xi d\zeta + \frac{X}{K_A}\int_0^1\int_0^\zeta F d\xi d\zeta, \tag{24}$$

and the ECM deformation is

$$U_E = \frac{1}{K_E}\int_0^X\int_0^\zeta F d\xi d\zeta - \frac{X}{K_E}\int_0^1 d\xi + A\sin(\omega t). \tag{25}$$

2.3 Initial conditions

For each amplitude of oscillatory loading, A, we consider two initial conditions: (i) a zero state with no pre-existing bound integrins, and (ii) a saturated steady state with high integrin binding, obtained in the absence of external forcing. In the discrete model, this is found by running the simulation with $A = 0$ until the fraction of bound integrins stabilises; in the continuum model the steady state, obtained from Eq. 13 when $V = 0$, is given by

$$b_s(x,0;X) = \frac{\eta k_b(x)}{k_u(x)}\left(\frac{1}{1 + \int_{-\infty}^\infty \frac{\eta k_b(x)}{k_u(x)}dx}\right). \tag{26}$$

3 Results

Effect of increasing the amplitude of oscillation

We first investigate the effect of varying the amplitude, A, of the oscillatory loading in both the discrete and continuum models. In Fig. 5 we show representative time courses from both models for the fraction of integrins that become fully-bound (B) under low, intermediate and high amplitude oscillatory loading. In the continuum model the total macroscale bound fraction is found from

$$B_{tot}(t) = \int_0^1 B(X,t)dX, \tag{27}$$

where $B(X,t)$ is given by Eq. 21.

For the lowest amplitude oscillation, in both models (Fig. 5(a)), we find that both the zero and saturated initial conditions converge to a pattern of high adhesion (with a mean total bound fraction of approximately 0.75) subject to small fluctuations as a result of a low, sustainable, turnover of bound integrins. For the highest amplitude loading (Fig. 5(c)), in both models and for both the zero and saturated initial conditions, the result is an oscillatory state in which significant bond rupture leads to a total bound integrin fraction with a lower mean (approximately 0.2–0.3) and larger amplitude fluctuations. For an intermediate oscillation amplitude (Fig. 5(b)) we observe bistability, where the initial condition determines which of the two adhesion states occur; if adhesions are present when oscillations begin, then shared loading and increased traction prevent high levels of rupture under applied strain. Due to the stochastic nature of the discrete model, under high amplitude oscillations we observe small variations in the time of collapse from the high to the low state. Similarly, it is possible to observe stochastic switching (not shown) between the two adhesion states when the loading parameter is within the bistable range. The high state exhibits persistence of bound integrins, whereas the low state shows cyclic breaking and reattachment of a significant fraction of integrins. These states could be akin to firm and transient adhesions, observed to occur in other contexts (see Discussion).
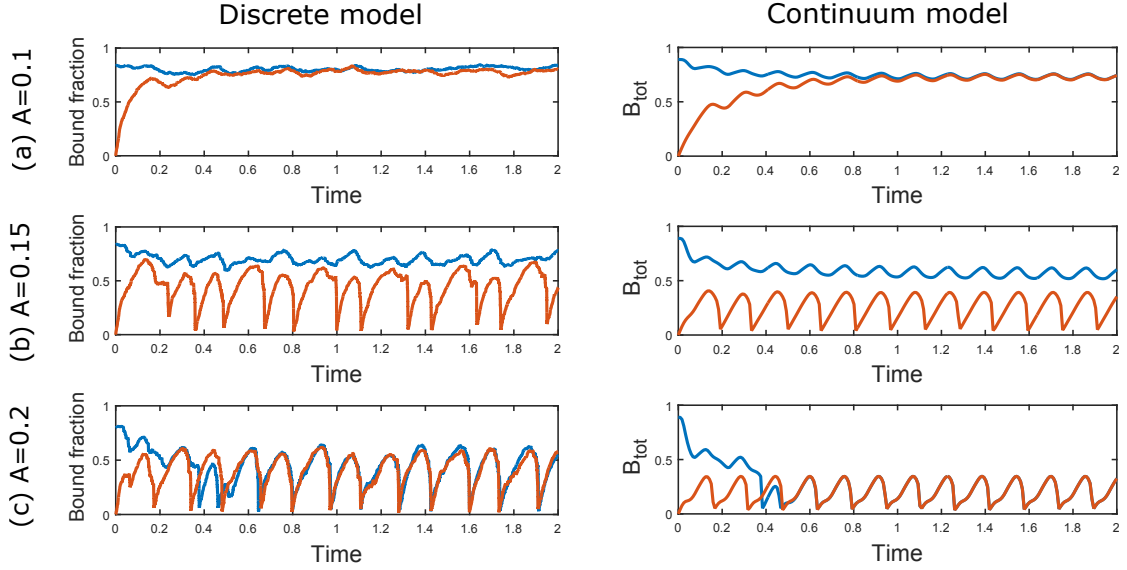
Figure 5: Representative time courses from the discrete stochastic simulation (Section 2.1) and continuum model (Section 2.2), shown in the left and right columns respectively, illustrating the responses of bound integrins (Eq. 27) to (a) low, (b) intermediate and (c) high amplitude oscillatory loading. This is applied using $\omega = 20$ and amplitudes $A = 0.1$, $A = 0.15$, and $A = 0.2$ respectively, via the boundary conditions in Eq. 4, or Eq. 18 (where Eq. 4 has been nondimensionalised using the scalings in Eqs. 12, 19). In each case we consider a zero (orange) and a saturated (blue) initial condition (Eq. 26). See Tables S1 and S2 in the Supporting Material for a full list of chosen parameter values.

As illustrated in Fig. 5, the discrete and continuum models display strikingly similar qualitative behaviour. We exploit the deterministic nature of the continuum model to more reliably investigate the bistability, summarised in Fig. 6, where we present the bound integrin densities obtained for a range of oscillation amplitudes. For each oscillation amplitude we use both the zero and saturated initial conditions. Since the states under consideration are oscillatory, once the behaviour has converged to its periodic steady state we plot the time-averaged adhesion density given by

$$\langle B(X) \rangle = \frac{1}{T} \int^{T} B(X, t) dt, \tag{28}$$

where $T = 2\pi/\omega$ is the oscillation period. There is variation in $\langle B(X) \rangle$ across the macroscale domain, $X \in [0, 1]$, and we observe a significantly lower adhesion density near $X = 0$ where the oscillation is applied.
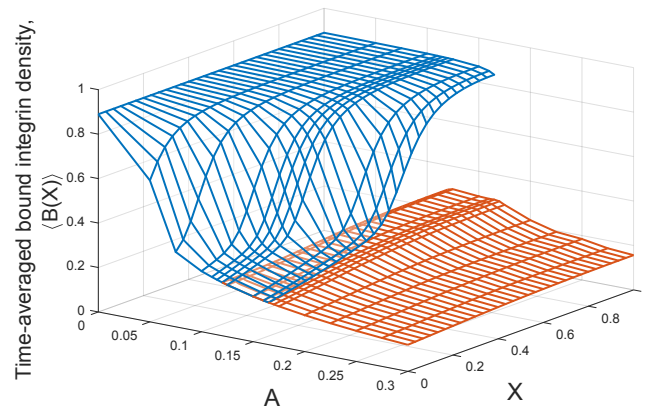

Figure 6: High (blue) and low (orange) solution surfaces across the macroscale domain, X, indicating stable states of the time-averaged adhesion density $\langle B(X) \rangle$ (Eq. 28) for a range of oscillation amplitudes, A (Eq. 18), in the continuum model. For intermediate amplitudes there is bistability. The model parameters are as in Fig. 5, and given in Table S1.

9

The time-averaged adhesion density plotted in Fig. 6, $\langle B(X) \rangle$, is additionally averaged over X to calculate the total time-averaged density $\langle B_{tot} \rangle$ (Eq. 27), which is used to generate a bifurcation diagram (Fig. 7). Stable branches, indicated by the solid lines, confirm, as in Fig. 6, that for low amplitude oscillations we expect solutions to converge to a high averaged bound integrin state regardless of initial conditions, while for high amplitude oscillations the solutions converge to a low bound integrin state. For an intermediate range of oscillation amplitudes we observe a window of bistability where the initial condition, in relation to an unstable branch (dashed line), determines which of the two stable outcomes occurs. The position of the unstable branch is estimated as the mean of two points that are observed to converge to the upper and lower solutions (green and red markers, respectively). The unstable and stable branches appear to meet in a pair of saddle node bifurcations. As illustrated in Fig. 7, starting on the upper stable branch, an increase in A would lead to a jump from the upper to the lower stable solution at the bifurcation point. The value of A at this point corresponds to a threshold loading at which adhesions quickly rupture. On the other hand a decrease in A from the lower branch leads to a jump from the lower to upper branch at a different amplitude, following a different path, thereby generating a hysteresis loop (blue dotted line).
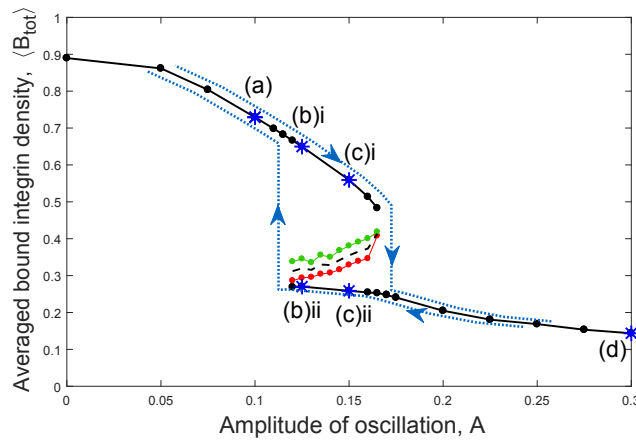

Figure 7: Bifurcation diagram indicating steady states of the time-averaged total adhesion density $\langle B_{tot} \rangle$ (Eqs. 27, 28) for a range of oscillation amplitudes, A (Eq. 18). Stable branches are indicated by solid lines separated by the dashed, unstable branch. The position of the unstable branch is bounded by points known to converge to the upper and lower solutions, in green and red respectively. Blue markers highlight example monostable ((a) $A = 0.1$, (d) $A = 0.3$) and bistable ((b) $A = 0.125$, (c) $A = 0.15$) regimes, and a hysteresis loop is seen (blue dotted line). The path taken as A increases ((a)→(b)i →(c)i→(d)) differs to the path followed as A decreases ((d)→(c)ii →(b)ii→(a)).

Next we examine the spatio-temporal cell deformation resulting from oscillatory loading for both the discrete and continuum models in each stable regime (Fig. 8). In the high bound integrin regime (i.e. low amplitude oscillations), adhesions persist and in both models there are smooth transitions between positive and negative cell deformations across the domain (Figs. 8(a), (c)). These appear as wide bands that follow the movement of the ECM. In the low bound integrin regime (high amplitude oscillations), the bands narrow and exhibit sharp boundaries due to greater numbers of rupture events at each cycle (Figs. 8(b), (d)). The differences in deformation that result from low and high amplitude oscillations correspond to differences in the total drag force generated by bound integrins, shown in Fig. 9. The total drag force in the continuum model, F_{tot}, is defined analogously to B_{tot} (Eq. 27). Note that, although the total drag forces are qualitatively similar in both models, there are some significant differences in the spatial propagation of the deformation applied at $X = 0$ (Fig. 8) because of the differences between the two modelling approaches. In particular, in the discrete model there are individual springs between each node, but this is simplified in the microscale formulation of the continuum model. Since bond rupture is affected by the level of deformation, the total bound fractions (Fig. 5) also differ slightly in magnitude between the two models; however, there is still striking qualitative agreement for the averaged macroscale quantities of interest (B_{tot}, F_{tot}, in Figs. 5, 9). Since we are primarily interested in qualitative behaviour, we exploit the efficiency of the continuum model in place of discrete stochastic simulations to investigate the effect of perturbations due to deep inspirations. We also investigate the effect of oscillation frequency, material stiffness and binding affinities on the averaged

bound integrin density, B_{tot} (Fig. S1 in the Supporting Material). In each case bistability is observed, but the positions of the stable branches are shifted.
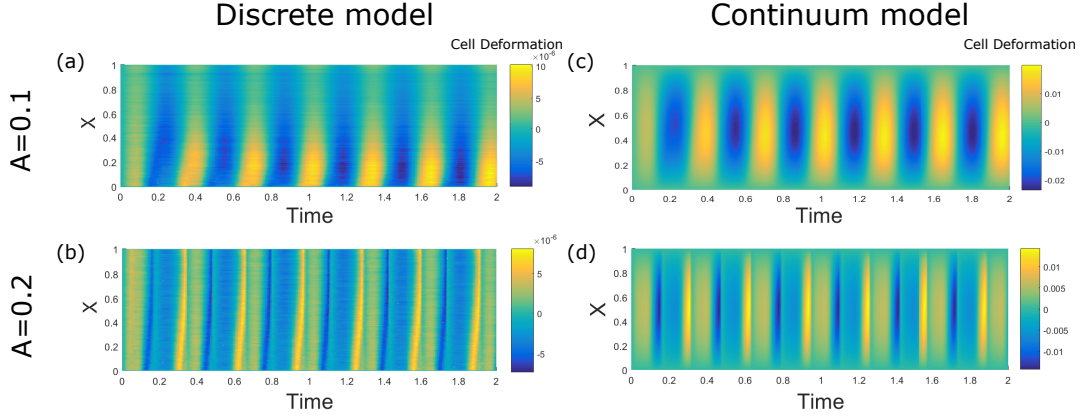

Figure 8: Cell deformation, $U_A(X, t)$, (indicated by colour) plotted as functions of the position in the cell domain, X, and time, t, obtained in the discrete (a,b) and continuum (c,d) models in the cases where adhesion formation (a,c) and adhesion rupture (b,d) dominate under oscillatory loading. Simulations are carried out from a zero initial condition, and oscillation amplitudes are $A = 0.1$ and $A = 0.2$ in Eq. 4 and Eq. 18. Eq. 4 has been nondimensionalised using the scalings in Eqs. 12, 19. In (a,b) the results have been averaged over 150 simulations, and the spatial positions are presented on a scaled domain $X \in [0, 1]$.
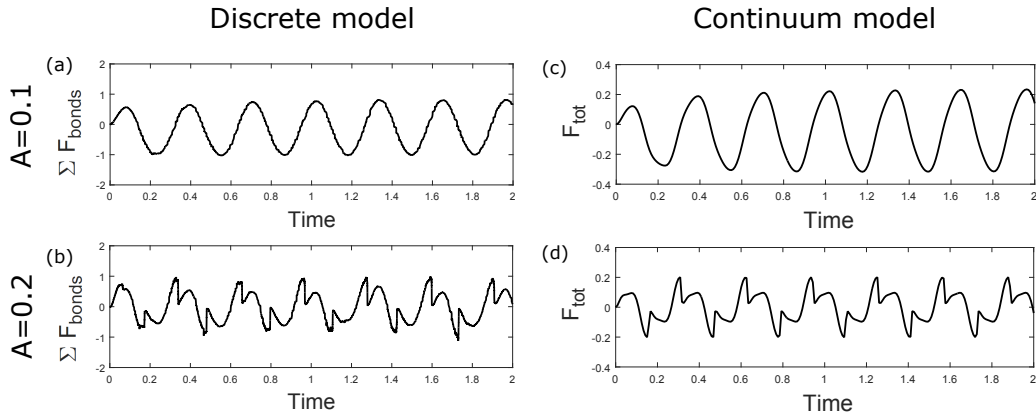

Figure 9: Total adhesive drag forces, F_{tot}, in the discrete (a,b) and continuum (c,d) models corresponding to the deformations in Fig. 8. (a,c). $A = 0.1$ in Eq. 4 and Eq. 18 and adhesion formation dominates. (b,d). $A = 0.2$ and there is increased rupture and a constant turnover of bound integrins under oscillatory loading. Eq. 4 has been nondimensionalised using the scalings in Eqs. 12, 19. As in Fig. 8, simulations are carried out from a zero initial condition. The results in (a,b) are from one sample discrete simulation.

Effect of perturbations due to deep inspirations

We now investigate the effect of transient perturbations to the amplitude of oscillatory loading, to mimic the strain imposed on ASM cells and ECM that may result from taking a deep inspiration (DI) during a period of regular breathing. Starting from the saturated initial condition (Eq. 26), we allow the bound fraction to settle to its periodic high steady state before perturbing the amplitude of the oscillation for one cycle. We therefore impose

$$U_E(0, t) = \begin{cases} A_2 \sin(\omega t), & \frac{8\pi}{\omega} < t < \frac{10\pi}{\omega}, \\ A_1 \sin(\omega t), & \text{otherwise}, \end{cases} \quad (29)$$

for baseline oscillation amplitude A_1, DI amplitude A_2 (where $A_2 > A_1$) and oscillation frequency $\frac{\omega}{2\pi}$.

We consider two different baseline oscillation amplitudes ($A_1 = 0.1$, $A_1 = 0.125$, marked by (a) and (b) in Fig. 7). This choice is motivated by variations in the amplitude of tidal breathing that may arise between individuals; pressure-driven oscillations *in vivo* lead to smaller strains for greater material stiffnesses (14, 47). The differences in A_1 could therefore correspond to asthmatic (stiff) and healthy (compliant) airways. We investigate the response to a small perturbation ($A_2 = 0.15$, point (c) in Fig. 7) and a DI that is large enough

to induce significant rupture of adhesions ($A_2 = 0.3$, point (d) in Fig. 7), and find that for a starting amplitude $A_1 = 0.1$, there is recovery to the high adhesion state regardless of the amplitude of the perturbation (Fig. 10(a)). For a starting amplitude $A_1 = 0.125$ there are two possible responses depending on the amplitude of the DI perturbation (Fig. 10(b)). As shown by the blue markers in Fig. 7, for $A_1 = 0.1$ the high adhesion state is the only stable solution and a high density of bound integrins therefore persists after a perturbation. In contrast, $A_1 = 0.125$ lies within the bistable window and if the DI perturbation is large enough to drive the system into the basin of attraction of the low adhesion state, there is a transition to a low bound integrin density which persists even after the oscillation returns to its initial amplitude.
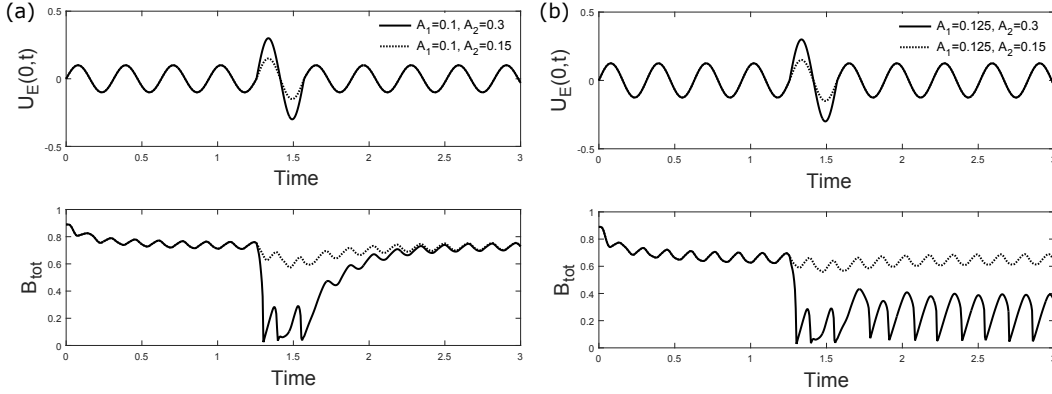

Figure 10: Different amplitude baseline oscillations and DI-like perturbations may lead to a switch in adhesion states. We show the applied oscillatory displacement, $U_E(0,t)$, and the total bound fraction of integrins, $B_{tot}(t)$, (see Eq. 29 and Eq. 27), when $\omega = 20$. (a) For $A_1 = 0.1$, $A_2 = 0.3$ (solid line) and $A_1 = 0.1$, $A_2 = 0.15$ (dashed line), the high adhesion state persists after both DI perturbations, since for $A_1 = 0.1$ this is the only steady state. (b) For $A_1 = 0.125$, $A_2 = 0.3$ (solid line), there is a transition to a low adhesion state, since $A_1 = 0.125$ is within the bistable window (see Fig. 7) and the DI is sufficiently large to drive the system into the basin of attraction of the low state. For a smaller amplitude perturbation, $A_2 = 0.15$ (dashed line), the high fraction of bound integrins persists.

These responses demonstrate the possible consequences of bistability as well as the importance of loading history, since an event such as a DI perturbation may alter the future state of adhesion when bistability is present. Persistence of the previous state depends on the amplitude of the DI and on where the bistable window (Fig. 7) lies in relation to the baseline oscillation amplitude, A_1. Physiologically, this will be influenced by differences in the amplitude of the baseline oscillatory displacement, representing tidal breathing, and differences in parameters such as the oscillation frequency, material stiffnesses and binding affinities which shift the location of the bistable window (Fig. S1).

4 Discussion

We have developed a discrete stochastic-elastic model and a multiscale continuum model in order to investigate the effect of oscillatory loading on the dynamics of ASM cell–matrix adhesions. We have demonstrated that oscillatory loading, representing deformations due to tidal breathing, can have a significant impact on integrin dynamics and the persistence of adhesions, which we expect to affect the level of force that can be transmitted between intracellular and extracellular domains. In particular, we observe two distinct regimes where either adhesion formation or adhesion rupture dominate, resulting in differences in the steady state densities of bound integrins (Fig. 5). Moreover, a window of bistability exists for intermediate loading amplitudes (Fig. 7) due to mechanical cooperativity; shared loading between pre-existing adhesions allows the high density state to persist when rupture would otherwise dominate. This bistability generates a hysteresis loop and we see that the loading history and events such as perturbations representing deep inspirations can significantly alter the future adhesion dynamics (Fig. 10). In previous studies (23, 48), similar instances of integrin cooperativity have been observed, where shared loading between integrins aids initial cluster formation. In addition to the differences in bound integrin densities seen in the two regimes, cell deformations and

adhesive drag forces also differ significantly in each case, both in terms of magnitude and dynamics (Figs. 8, 9). The qualitative behaviours seen in the discrete model are also observed in our continuum model, the convenience of which we exploit to investigate the adhesion dynamics further. The existence of a threshold at which bond rupture dominates over adhesion formation is in agreement with the Monte Carlo simulations in a previous study (22), where an oscillatory strain is applied to an initially fully-bound substrate. Our model assumptions differ in some respects to those of Kong *et al.* (22), but sudden rupture occurs in both when the oscillation amplitude is increased. In our model, we additionally observe bistability and hysteresis. The two adhesion states reported appear to behave similarly to transient and firm adhesions, observed in other contexts. Integrin-mediated adhesions can function as either dynamic or stable structures (6) and, in the context of cell migration, switching between transient and firm adhesion states (mediated by biochemical signalling) facilitates migration by altering the traction properties between cells and the ECM. As well as biochemical signals, mechanical signals are known to be able to modulate focal adhesion size and dynamics (49), and further studies into how the mechanical environment of ASM affects focal adhesions will be worthwhile.

We propose the following *in vitro* experiment to investigate whether the mechanical cooperativity of integrins could indeed lead to bistability: using atomic force microscopy, vertical or lateral oscillations could be applied to ECM–coated beads which initially have different but controlled levels of adhesion to the cell. Control over the initial condition can be achieved by varying the contact time between the bead and cell, as previously carried out in (50). In addition, by gradually increasing and then decreasing the amplitude of oscillation, the hysteresis illustrated in Figure 7 could be tested.

The airway response to DIs is known to be different in asthmatics and non-asthmatics: in healthy subjects DIs promote bronchodilation, but this effect is either transient or non-existent in asthmatics (9–11). DI-induced bronchodilation has previously been attributed to disruption of actin-myosin crossbridges (11), which mediate contractile force generation within the cell. However, since intracellular contractile force transmission to the extracellular domain is reliant on cell–matrix adhesions, the density of adhesions that survive under oscillatory loading in each case could also play an important role: we expect the high and low density adhesion states predicted by the model to produce significantly different levels of strain transmission between contracted ASM cells and the ECM. Our results show either persistence of the high adhesion state or a transition from the high to low adhesion states in response to DI-like perturbations (Fig. 10). The ability of a DI to induce a switch between states is influenced by a difference in either: (i) the position of the bistable region, which shifts in response to changes in parameters such as oscillation frequency, material stiffnesses and binding affinities (see Fig. S1 in the Supporting Material); (ii) the amplitude of the unperturbed oscillatory displacement, which we use to represent the magnitude of tidal breathing; or (iii) the magnitude of the DI. All of these factors could differ between individuals, as well as between asthmatics and non-asthmatics. To fully understand the bronchodilatory effect of DIs, it will be crucial to consider the combined dynamics of actin-myosin crossbridges and integrins; we expect them both to contribute, but their relative importance will only become clear when considered together. Although actin-myosin crossbridge cycling, which mediates contractile force generation within the cell, undergoes changes during DIs, by considering the possible integrin response to breathing and DIs we have illustrated that strain transmission (via integrins) could also be a highly dynamic process. Integrin–mediated adhesion is therefore an important process to study further in this context.

Further motivation for understanding contractile force transmission between ASM cells and the ECM in the context of asthma is that contractile force is also known to promote the activation of TGFβ, a growth factor which otherwise remains latent in the ECM. TGFβ promotes long term airway remodelling with consequences such as airway wall thickening and altered material properties (e.g. increased stiffness) of the airway tissue (51–55). These structural changes are irreversible and over time lead to obstructed airflow and a decline in lung function. In order to fully understand the effect of cell–matrix adhesion density on levels of contractile force transmission, and the consequences that this may have for the activation of TGFβ, future work will involve an extension to higher dimensions where the constraint on vertical motion will be relaxed. This is an important step towards a full coupling to models of actomyosin dynamics and contractile force generation in ASM cells.

Our results were obtained firstly in a stochastic-elastic computational model and then in a continuum model. We find that our discrete and continuum models produce similar qualitative behaviour, and in a future study we will consider the formal relationship between the two models. This will allow for more rigorous quantitative, as well as qualitative, comparisons. Whilst the discrete model is advantageous for incorporating large amounts of individual detail, the continuum model can more easily be coupled to existing models of contractile force generation, for example (56), and is more efficient when the number of integrins is high. In (56), crossbridge cycling and disruption to actin-myosin contractile units (in response to cell length changes) are considered, which would allow us to more fully investigate the combined dynamics of crossbridges and integrins during DIs. The continuum model can additionally be extended to address simplifications made during initial model development; in particular, we can consider nonlinear elastic materials in order to accommodate large deformations, a more complete reaction sequence including integrin diffusion and activation, and different forms for spatial binding and rupture rates. Instead of our simplified piecewise linear rates, a more commonly used description for bond rupture under force is the Bell model (57), in which rupture rates increase exponentially with force. Other rate functions, including a power law relation, have also been presented (58, 59), and obtaining precise measurements for individual integrins, using techniques such as atomic force microscopy (60), remains an area of ongoing research. As we explicitly account for binding and unbinding rates that depend on microscale distance, both our discrete and continuum models can accommodate any of these choices.

Here we have discussed cell–matrix adhesion in the context of tidal breathing and airway smooth muscle. However, the models presented could be applicable to other contexts where dynamic environments occur. Interesting examples include the adhesion dynamics that occur in response to large volume changes in the urinary bladder or in uterine smooth muscle during pregnancy and childbirth. In both of these cases, it is thought that integrins play an important role in the adaptation of smooth muscle to different lengths and functions (61, 62).

In this paper we have shown that cell–matrix adhesion strength can be heavily influenced by dynamic loading (representing tidal breathing and DIs) and by the loading history. To date, consideration of mechanical ASM-ECM interactions via integrins has been neglected in investigations on the effect of tidal breathing and DIs in asthma. Here we have shown that integrins could play an important role in the level of strain transmission during ASM contraction *in vivo*, since the bound integrin density responds dynamically to oscillatory loading. Furthermore, a simulated DI is shown to induce either transient or permanent changes in the bound integrin density, depending on the amplitude of tidal breathing (Fig. 10). This result could help to explain, in part, previous experimental observations on the bronchodilatory effect of DIs, which are transient or absent in asthmatics yet sustained in healthy subjects.

AUTHOR CONTRIBUTIONS

M.R.O, R.D.O, B.S.B designed research; L.I performed research; L.I, M.R.O, R.D.O, B.S.B analysed data; L.I prepared figures; L.I, M.R.O, R.D.O, B.S.B drafted manuscript; L.I, M.R.O, R.D.O, B.S.B edited and revised manuscript.

ACKNOWLEDGEMENTS

References

1. Bousquet, J., P. K. Jeffery, W. W. Busse, M. Johnson, and A. M. Vignola, 2000. Asthma: from bronchoconstriction to airways inflammation and remodeling. *American Journal of Respiratory and Critical Care Medicine* 161:1720–1745.

2. Gunst, S. J., D. D. Tang, and A. O. Saez, 2003. Cytoskeletal remodeling of the airway smooth muscle cell: a mechanism for adaptation to mechanical forces in the lung. *Respiratory physiology & neurobiology* 137:151–168.

3. Zhang, W., and S. J. Gunst, 2008. Interactions of airway smooth muscle cells with their tissue matrix: implications for contraction. *Proceedings of the American Thoracic Society* 5:32–39.

4. Hynes, R. O., 2002. Integrins: bidirectional, allosteric signaling machines. *Cell* 110:673–687.

5. Schwartz, M. A., 2010. Integrins and extracellular matrix in mechanotransduction. *Cold Spring Harbor perspectives in biology* 2:a005066.

6. Hoffman, B. D., C. Grashoff, and M. A. Schwartz, 2011. Dynamic molecular processes mediate cellular mechanotransduction. *Nature* 475:316–323.

7. Sun, Z., S. Guo, and R. Fässler, 2016. Integrin-mediated mechanotransduction. *The Journal of Cell Biology* 215.

8. Wolfenson, H., I. Lavelin, and B. Geiger, 2013. Dynamic Regulation of the Structure and Functions of Integrin Adhesions. *Developmental Cell* 24:447–458.

9. Kapsali, T., S. Permutt, B. Laube, N. Scichilone, and A. Togias, 2000. Potent bronchoprotective effect of deep inspiration and its absence in asthma. *Journal of Applied Physiology* 89:711–720.

10. Crimi, E., R. Pellegrino, M. Milanese, and V. Brusasco, 2002. Deep breaths, methacholine, and airway narrowing in healthy and mild asthmatic subjects. *Journal of Applied Physiology* 93:1384–1390.

11. Scichilone, N., T. Kapsali, S. Permutt, and A. Togias, 2000. Deep inspiration-induced bronchoprotection is stronger than bronchodilation. *American Journal of Respiratory and Critical Care Medicine* 162:910–916.

12. Gunst, S. J., 1983. Contractile force of canine airway smooth muscle during cyclical length changes. *Journal of Applied Physiology* 55:759–769.

13. Latourelle, J., B. Fabry, and J. J. Fredberg, 2002. Dynamic equilibration of airway smooth muscle contraction during physiological loading. *Journal of Applied Physiology* 92:771–779.

14. LaPrad, A. S., T. L. Szabo, B. Suki, and K. R. Lutchen, 2010. Tidal stretches do not modulate responsiveness of intact airways in vitro. *Journal of applied physiology* 109:295–304.

15. Bates, J., 2015. Modeling the impairment of airway smooth muscle force by stretch. *Journal of Applied Physiology* 118:684–691.

16. Campbell, I. D., and M. Ginsberg, 2004. The talin–tail interaction places integrin activation on FERM ground. *Trends in Biochemical Sciences* 29:429–435.

17. Banno, A., and M. H. Ginsberg, 2008. Integrin activation. *Biochemical Society Transactions* 36:229–234.

18. Seifert, U., 2000. Rupture of multiple parallel molecular bonds under dynamic loading. *Physical review letters* 84:2750–2753.

19. Erdmann, T., and U. S. Schwarz, 2004. Stability of adhesion clusters under constant force. *Physical Review Letters* 92:108102.

20. Erdmann, T., and U. S. Schwarz, 2006. Bistability of cell-matrix adhesions resulting from nonlinear receptor-ligand dynamics. *Biophysical journal* 91:L60–L62.

21. Qian, J., J. Wang, Y. Lin, and H. Gao, 2009. Lifetime and strength of periodic bond clusters between elastic media under inclined loading. *Biophysical Journal* 97:2438–2445.

22. Kong, D., B. Ji, and L. Dai, 2008. Stability of adhesion clusters and cell reorientation under lateral cyclic tension. *Biophysical journal* 95:4034–44.

23. Paszek, M. J., D. Boettiger, V. M. Weaver, and D. A. Hammer, 2009. Integrin clustering is driven by mechanical resistance from the glycocalyx and the substrate. *PLoS Computational Biology* 5.

24. Hammer, D. A., and S. M. Apte, 1992. Simulation of cell rolling and adhesion on surfaces in shear flow: general results and analysis of selectin-mediated neutrophil adhesion. *Biophysical journal* 63:35–57.

25. Hammer, D. A., 2014. Adhesive dynamics. *Journal of biomechanical engineering* 136:021006.

26. Chan, C. E., and D. J. Odde, 2008. Traction dynamics of filopodia on compliant substrates. *Science* 322:1687–1691.

27. Walcott, S., D.-H. Kim, D. Wirtz, and S. X. Sun, 2011. Nucleation and decay initiation are the stiffness-sensitive phases of focal adhesion maturation. *Biophysical journal* 101:2919–2928.

28. Filippov, A. E., J. Klafter, and M. Urbakh, 2004. Friction through dynamical formation and rupture of molecular bonds. *Physical Review Letters* 92:135503–1.

29. Srinivasan, M., and S. Walcott, 2009. Binding site models of friction due to the formation and rupture of bonds: State-function formalism, force-velocity relations, response to slip velocity transients, and slip stability. *Physical Review E - Statistical, Nonlinear, and Soft Matter Physics* 80:1–15.

30. Lacker, H. M., and C. S. Peskin, 1986. A mathematical method for unique determination of crossbridge properties from steady-state mechanical and energetic experiments on macroscopic muscle. *In* Some Mathematical Questions in Biology–Muscle Physiology, The American Mathematical Society, Providence, RI, volume 16, 121–153.

31. Wiseman, P. W., C. M. Brown, D. J. Webb, B. Hebert, N. L. Johnson, J. A. Squier, M. H. Ellisman, and A. F. Horwitz, 2004. Spatial mapping of integrin interactions and dynamics during cell migration by image correlation microscopy. *Journal of cell science* 117:5521–5534.

32. Welf, E. S., U. P. Naik, and B. A. Ogunnaike, 2012. A spatial model for integrin clustering as a result of feedback between integrin activation and integrin binding. *Biophysical Journal* 103:1379–1389.

33. Block, M. R., O. Destaing, C. Petropoulos, E. Planus, C. Albigès-Rizo, and B. Fourcade, 2015. Integrin-mediated adhesion as self-sustained waves of enzymatic activation. *Physical Review E* 92:042704.

34. Cao, X., Y. Lin, T. P. Driscoll, J. Franco-Barraza, E. Cukierman, R. L. Mauck, and V. B. Shenoy, 2015. A chemomechanical model of matrix and nuclear rigidity regulation of focal adhesion size. *Biophysical journal* 109:1807–1817.

35. Cao, X., E. Ban, B. M. Baker, Y. Lin, J. A. Burdick, C. S. Chen, and V. B. Shenoy, 2017. Multiscale model predicts increasing focal adhesion size with decreasing stiffness in fibrous matrices. *Proceedings of the National Academy of Sciences* 201620486.

36. Maraldi, M., C. Valero, and K. Garikipati, 2014. A computational study of stress fiber-focal adhesion dynamics governing cell contractility. *Biophysical journal* 106:1890–1901.

37. Deshpande, V. S., M. Mrksich, R. M. McMeeking, and A. G. Evans, 2008. A bio-mechanical model for coupling cell contractility with focal adhesion formation. *Journal of the Mechanics and Physics of Solids* 56:1484–1510.

38. Nicolas, A., B. Geiger, and S. A. Safran, 2004. Cell mechanosensitivity controls the anisotropy of focal adhesions. *Proceedings of the National Academy of Sciences of the United States of America* 101:12520–12525.

39. Gao, H., J. Qian, and B. Chen, 2011. Probing mechanical principles of focal contacts in cell-matrix adhesion with a coupled stochastic-elastic modelling framework. *Journal of the Royal Society, Interface / the Royal Society* 8:1217–1232.

40. Huxley, A. F., 1957. Muscle structure and theories of contraction. *Prog. Biophys. Biophys. Chem.* 7:255–318.

41. Gillespie, D. T., 1977. Exact Stochastic Simulation of Coupled Chemical Reactions. *The Journal of Physical Chemistry* 81:2340–2361.

42. Hill, T. L., 1974. Theoretical formalism for the sliding filament model of contraction of striated muscle Part I. *Progress in biophysics and molecular biology* 28:267–340.

43. Bates, J. H. T., S. R. Bullimore, A. Z. Politi, J. Sneyd, R. C. Anafi, and A. M. Lauzon, 2009. Transient oscillatory force-length behavior of activated airway smooth muscle. *American Journal of Physiology-Lung Cellular and Molecular Physiology* 297:L362–L372.

44. Harvey, B. C., H. Parameswaran, and K. R. Lutchen, 2013. Can tidal breathing with deep inspirations of intact airways create sustained bronchoprotection or bronchodilation? *Journal of applied physiology* 115:436–445.

45. Mailhot-Larouche, S., K. Lortie, D. Marsolais, N. Flamand, and Y. Bossé, 2017. An in vitro study examining the duration between deep inspirations on the rate of renarrowing. *Respiratory physiology & neurobiology* 243:13–19.

46. Raqeeb, A., D. Solomon, P. D. Paré, and C. Y. Seow, 2010. Length oscillation mimicking periodic individual deep inspirations during tidal breathing attenuates force recovery and adaptation in airway smooth muscle. *Journal of Applied Physiology* 109:1476–1482.

47. Hiorns, J. E., O. E. Jensen, and B. S. Brook, 2014. Nonlinear compliance modulates dynamic bronchoconstriction in a multiscale airway model. *Biophysical journal* 107:3030–3042.

48. Selhuber-Unkel, C., M. López-García, H. Kessler, and J. P. Spatz, 2008. Cooperativity in adhesion cluster formation during initial cell adhesion. *Biophysical journal* 95:5424–5431.

49. Na, S., A. Trache, J. Trzeciakowski, Z. Sun, G. A. Meininger, and J. D. Humphrey, 2008. Time-dependent changes in smooth muscle cell stiffness and focal adhesion area in response to cyclic equibiaxial stretch. *Annals of Biomedical Engineering* 36:369–380.

50. Sun, Z., L. A. Martinez-Lemus, A. Trache, J. P. Trzeciakowski, G. E. Davis, U. Pohl, and G. A. Meininger, 2005. Mechanical properties of the interaction between fibronectin and $\alpha5\beta1$-integrin on vascular smooth muscle cells studied using atomic force microscopy. *American Journal of Physiology-Heart and Circulatory Physiology* 289:H2526–H2535.

51. Tatler, A. L., A. E. John, L. Jolly, A. Habgood, J. Porte, C. Brightling, A. J. Knox, L. Pang, D. Sheppard, X. Huang, and G. Jenkins, 2011. Integrin $\alpha v\beta5$-Mediated TGFβ Activation by Airway Smooth Muscle Cells in Asthma. *The Journal of Immunology* 187:6094–6107.

52. Oenema, T. A., H. Maarsingh, M. Smit, G. M. M. Groothuis, H. Meurs, and R. Gosens, 2013. Bronchoconstriction Induces TGFβ Release and Airway Remodelling in Guinea Pig Lung Slices. *PLoS ONE* 8.

53. Elias, J. A., Z. Zhu, G. Chupp, and R. J. Homer, 1999. Airway remodeling in asthma. *The Journal of Clinical Investigation* 104:1001–1006.

54. James, A. L., and S. Wenzel, 2007. Clinical relevance of airway remodelling in airway diseases. *European Respiratory Journal* 30:134–155.

55. Pascual, R. M., and S. P. Peters, 2005. Airway remodeling contributes to the progressive loss of lung function in asthma: An overview. *Journal of Allergy and Clinical Immunology* 116:477 – 486.

56. Brook, B. S., 2014. Emergence of airway smooth muscle mechanical behavior through dynamic reorganization of contractile units and force transmission pathways. *Journal of Applied Physiology* 116:980–997.

57. Bell, G. I., 1978. Models for the Specific Adhesion of Cells to Cells. *Science* 200:618–627.

58. Evans, E., D. Berk, and A. Leung, 1991. Detachment of agglutinin-bonded red blood cells. I. Forces to rupture molecular-point attachments. *Biophysical journal* 59:838–848.

59. Evans, E., and K. Ritchie, 1997. Dynamic strength of molecular adhesion bonds. *Biophysical journal* 72:1541–1555.

60. Franz, C. M., A. Taubenberger, P. Puech, and D. J. Muller, 2007. Studying integrin-mediated cell adhesion at the single-molecule level using AFM force spectroscopy. *Sci. Stke* 2007:pl5.

61. Wilson, C. B., J. Leopard, D. A. Cheresh, and R. M. Nakamura, 1996. Extracellular matrix and integrin composition of the normal bladder wall. *World journal of urology* 14:S30–S37.

62. Williams, S. J., B. G. White, and D. J. MacPhee, 2005. Expression of $\alpha5$ integrin (Itga5) is elevated in the rat myometrium during late pregnancy and labor: Implications for development of a mechanical syncytium. *Biology of reproduction* 72:1114–1124.

63. Li, F., S. D. Redick, H. P. Erickson, and V. T. Moy, 2003. Force measurements of the $\alpha 5 \beta 1$ integrin–fibronectin interaction. *Biophysical journal* 84:1252–1262.

64. Selhuber-Unkel, C., T. Erdmann, M. Lopez-Garcia, H. Kessler, U. S. Schwarz, and J. P. Spatz, 2010. Cell adhesion strength is controlled by intermolecular spacing of adhesion receptors. *Biophysical journal* 98:543–551.

65. Nermut, M. V., N. M. Green, P. Eason, S. S. Yamada, and K. M. Yamada, 1988. Electron microscopy and structural model of human fibronectin receptor. *The EMBO journal* 7:4093–4099.

66. Lepzelter, D., O. Bates, and M. Zaman, 2012. Integrin clustering in two and three dimensions. *Langmuir* 28:5379–5386.

67. Kong, D., B. Ji, and L. Dai, 2010. Stabilizing to disruptive transition of focal adhesion response to mechanical forces. *Journal of Biomechanics* 43:2524–2529.

68. Williams, E. M., T. Powell, M. Eriksen, P. Neill, and R. Colasanti, 2014. A pilot study quantifying the shape of tidal breathing waveforms using centroids in health and COPD. *Journal of clinical monitoring and computing* 28:67–74.

69. Hughes, P. E., and M. Pfaff, 1998. Integrin affinity modulation. *Trends in cell biology* 8:359–364.

Effect of loading history on airway smooth muscle cell–matrix adhesions: Supporting material

Linda Irons, Markus R. Owen, Reuben D. O'Dea, Bindi S. Brook

Centre for Mathematical Medicine and Biology, School of Mathematical Sciences, University of

Nottingham, Nottingham, NG7 2RD, UK

Here we present further details about the numerical simulation of the discrete and continuum models (Section S.1), a list of the parameter values used (Section S.2), and additional figures to support and extend the continuum model results in Section 3 of the main text (Section S.3).

S.1   Numerical methods

Both models were implemented in MATLAB 2016b, as detailed below.

S.1.1   Discrete simulations

The algorithm employed in the discrete stochastic–elastic simulations (see Section 2.1) is summarised as follows. We employ a first reaction method (41) to select the stochastic binding and unbinding reactions.

Algorithm S1 Discrete stochastic–elastic model

1: Initialise actin and ECM spring networks and relax to mechanical equilibrium.
2: **while** $\hat{t} < \hat{T}$ **do**
3: Calculate binding and unbinding propensities, a_i, based on pairwise distances (where $i \in [1, ...N]$ and N denotes the number of possible reactions).
4: Generate a uniformly distributed random number, r_1, from the interval $(0, 1)$, to calculate the time elapsed before the next reaction, $\hat{\tau} = \frac{1}{a_0}\ln(1/r_1)$. The constant a_0 is the sum of all reaction propensities, $a_0 = \sum_{i=1}^{N} a_i$.
5: **if** $\hat{\tau} < \hat{\tau}_{max}$ **then**
6:   Generate a second uniformly distributed random number, $r_2 \in (0, 1)$, and select the reaction, indexed by μ, such that $\sum_{i=1}^{\mu-1} a_i < a_0 r_2 \leq \sum_{i=1}^{\mu} a_i$ is satisfied.
7:   Update the structure of the spring network according to chosen reaction.
8: **end if**
9: Set $\hat{t} = \hat{t} + \min\{\hat{\tau}, \hat{\tau}_{max}\}$. Calculate net forces acting on each point, and update positions by solving $\Sigma \hat{\boldsymbol{F}}_i = \boldsymbol{0}$
10: **end while**

S.1.2   Continuum simulations

In the continuum model (see Section 2.2), we solve a microscale advection–reaction system (Eq. 13) coupled to a second order macroscale PDE (Eq. 20). The macroscale PDE is solved using a finite difference scheme, subject to the boundary conditions in Eq. 23.

We discretise the macroscale domain, $X \in [0, 1]$, into N points with an equal spacing of $\Delta X = 1/(N-1)$. Macroscale variables V, H, and B (defined in Eqs. 8, 21) are discretised into the vectors $\boldsymbol{v} = (V_1, V_2, ..., V_N)^T$, $\boldsymbol{h} = (H_1, H_2, ..., H_N)^T$, and $\boldsymbol{b} = (B_1, B_2, ..., B_N)^T$, respectively, where the built-in MATLAB function `trapz` is used in calculating the elements of $\boldsymbol{h}$ and $\boldsymbol{b}$ from microscale distributions (see Eq. 21).

By using a second order central difference in Eq. 20, we solve for $\boldsymbol{v}$ through a matrix equation of the form

$$\boldsymbol{v} = \boldsymbol{A}^{-1}\boldsymbol{p}, \tag{S1}$$

where the vector $\boldsymbol{p}$ is given by

$$\boldsymbol{p} = (\alpha\omega\cos(\omega t), \gamma H_2, ..., \gamma H_N)^T, \tag{S2}$$

and the matrix $\boldsymbol{A}$ is

$$\boldsymbol{A} = \begin{pmatrix} 1 & 0 & 0 & 0 & 0 & \dots & 0 \\ \frac{1}{\Delta X^2} & D_2 & \frac{1}{\Delta X^2} & 0 & 0 & \dots & 0 \\ 0 & \frac{1}{\Delta X^2} & D_3 & \frac{1}{\Delta X^2} & 0 & \dots & 0 \\ \vdots & \ddots & \ddots & \ddots & \ddots & \ddots & \vdots \\ 0 & \dots & 0 & \frac{1}{\Delta X^2} & D_{N-2} & \frac{1}{\Delta X^2} & 0 \\ 0 & \dots & 0 & 0 & \frac{1}{\Delta X^2} & D_{N-1} & \frac{1}{\Delta X^2} \\ 0 & \dots & 0 & 0 & 0 & \frac{2}{\Delta X^2} & D_N \end{pmatrix}. \tag{S3}$$

The diagonal elements, $D_2, ..., D_N$, are given by $D_i = -\frac{2}{\Delta X^2} - \frac{\gamma}{\delta}B_i$, for $i \in \{2, ..., N\}$, where B_i are elements of the discretised bound fraction vector, $\boldsymbol{b}$, as defined above. Eq. S1 is solved alongside the microscale advection–reaction system (Eq. 13), for which we evolve discretised microscale distributions, $b(x, t; X)$, using the built-in MATLAB function `ode15s` with a first order upwind scheme for the spatial derivatives. We evolve microscale distributions at each of the N (macroscale) discretised points, and distributions are coupled through the solution of $\boldsymbol{v}$.

S.2 Parameter values

S.2.1 Dimensionless parameter values

Dimensionless parameter values used in the continuum and discrete simulations, unless otherwise stated in figure captions, are given below.

Parameter	Description	Value
K_A	Cell Stiffness	2
K_E	ECM Stiffness	4
h	Integrin binding range	1
s	Maximum integrin range	1.5
h_1	Dimensionless unbinding parameter (Eq. 15)	0.5
h_2	Dimensionless unbinding parameter (Eq. 15)	0.4
h_3	Dimensionless unbinding parameter (Eq. 15)	5000
δ	Ratio of microscale binding range, $\hat{h}$, to macroscale lengthscale $\hat{L}$	0.05
ν	Ratio of microscale binding range, $\hat{h}$, to microscale characteristic length, $\hat{l}$.	5
ω	Frequency of oscillatory loading	20

Table S1: Dimensionless parameter values for the continuum simulations, unless otherwise stated in figures.

Parameter	Description	Value
N_{I_A}	Number of I_A nodes	300
N_E	Number of E nodes	500
κ_a	Cell Spring Constant	$2(N_{I_A}\text{-}1)$
κ_r	Restoring Spring Constant	$2(N_{I_A}\text{-}1)$
κ_e	ECM Spring Constant	$4(N_E\text{-}1)$
κ_b	Integrin Spring Constant	1.8
h	Integrin binding range	1
s	Maximum integrin range	1.5
h_1	Dimensionless unbinding parameter (Eq. 15)	0.5
h_2	Dimensionless unbinding parameter (Eq. 15)	0.4
h_3	Dimensionless unbinding parameter (Eq. 15)	5000
δ	Ratio of microscale binding range, $\hat{h}$, to macroscale lengthscale $\hat{L}$	0.05
ω	Frequency of oscillatory loading	20

Table S2: Parameter values for the discrete simulations, unless otherwise stated in figures. Note that the cell and ECM spring constants are scaled by $(N_{I_A}\text{-}1)$ and $(N_E\text{-}1)$, respectively, which are the number of cell and ECM springs that act in series between $X = 0$ and $X = 1$ (see Fig. 2).

S.2.2 Dimensional parameter values

The above dimensionless parameters were obtained, where possible, by using dimensional values from the literature (see below). Some parameters were unknown or widely variable in the literature (denoted by **) and are discussed further below.

Parameter	Description	Range of values	Sources	Chosen value
$\hat{T}$	Breathing cycle duration	$2.7 - 5.8$s	(68)	3.9s
$\hat{\omega}$	Frequency (angular) of oscillatory loading	$1.08 - 2.33\text{s}^{-1}$	From $\hat{\omega} = 2\pi/\hat{T}$	1.6s^{-1}
$\hat{g}_1$	Unstressed unbinding rate	$0.012 - 0.04\text{s}^{-1}$	(63), (64)	0.04s^{-1}
$\hat{g}_2$	Unbinding parameter			0.032s^{-1**}
$\hat{g}_3$	Forced unbinding rate	Instantaneous	Model choice	400s^{-1}
$\hat{f}_1$	Unstressed binding rate	$0.015 - 1.5\text{s}^{-1}$	(64), (32)	0.08s^{-1**}
$\hat{h}$	Integrin binding range	$0 - 28$nm	(65)	20nm
$\hat{s}$	Maximum integrin range before unbinding	28nm+	(65)	30nm
$\hat{\lambda}_b$	Integrin spring constant	$0.15 - 2$pN/nm	(37), (39), (23)	0.15pN/nm
$\hat{\rho}$	Number of integrins per unit length	$0 - 0.2\text{nm}^{-1}$	(66)	0.1nm^{-1**}
$\hat{l}$	Characteristic length			4nm
$\hat{L}$	Characteristic length			400nm

Table S3: Dimensional parameter values used to obtain the dimensionless values in Table S1. Parameters that were unknown or widely variable in the literature are denoted by ** and are discussed further below.

The unstressed binding rate $\hat{f}_1$ varies widely in the literature, as it depends on a number of factors including integrin affinity, integrin density and ligand density. Here we have chosen a rate based on (32, 64); however, higher values have also been used in the simulations of (23, 67). The unbinding parameter, $\hat{g}_2$, used in the piecewise linear rates (Eq. 3) does not have an equivalent in the literature, and was chosen to be of the same order of magnitude as the other reaction rates, $\hat{g}_1$ and $\hat{f}_1$. Some parameter values were estimated from known properties of integrins. The integrin binding ranges, $\hat{h}$ and $\hat{s}$ are estimates based on the length of integrins.

An upper bound for $\hat{\rho}$ is estimated based on integrin diameters, which are typically between 5-10nm (66). This suggests a maximum value of $\hat{\rho} = 0.2\text{nm}^{-1}$; however, the integrin density will vary up to this value depending on the extent of integrin clustering.

The constants $\hat{K}_A$ and $\hat{K}_E$ in Eq. 9 are given values (240pN and 480pN respectively) such that the dimensionless stiffness parameters, K_A and K_E in Eq. 17, are $\mathcal{O}(1)$. We make this choice so that the drag arising from bound integrins, $F(X, t)$, influences the macroscale dynamics via Eq. 17, since integrins are known to be able to influence cell and ECM deformation.

Naturally there is some uncertainty associated with the above parameters, and we have investigated the effect of varying some of these. We find that the qualitative behaviours reported in the main text appear for a range of parameter values, with some examples discussed in Section S.3.1 and shown in Figs. S11 and S12.

S.3   Additional simulations

Using the continuum model, we can also investigate the effect of varying the oscillation frequency, material stiffnesses, and binding affinities (Section S.3.1). We show that these parameters affect the position and width of the bistable region, and demonstrate that the dynamics we observe can be found for a range of parameter values. In Section S.3.2, we will consider the effect of varying the waveform representing tidal breathing since, in reality, this will not be perfectly sinusoidal.

S.3.1   Effect of varying the model parameters

We first consider the effect of varying the oscillation frequency. An increase in the frequency of applied oscillations results in a decrease in the averaged bound integrin density, $\langle B_{tot} \rangle$, on both stable branches (Fig. S1(a)). This is due to reduced contact times for integrin binding. The most significant shift occurs in the lower branch where rupture and rebinding must occur at each cycle; the increased frequency prevents significant binding. The location and size of the bistable window are also affected; for increased frequencies the lower branch persists for lower amplitudes, A, and the bistable region widens. The end points of the high and low branches have been calculated (to the nearest 0.005), giving the widths of the bistable region to be in the ranges $[0.03, 0.04]$, $[0.045, 0.055]$, and $[0.055, 0.065]$ for $\omega = 10, 20$, and 30 respectively.

The material stiffnesses K_A and K_E influence the microscale distributions through the parameter γ that appears in the macroscale relative velocity (Eqs. 20, 21). As seen by Eq. 21, the value of γ decreases when either K_A or K_E are increased; similarly, γ increases when either K_A or K_E are reduced. Without loss of generality, in Fig. S1(b) we present results corresponding to variations in K_A. We observe that an increased cell or ECM stiffness (i.e. reduced γ) leads to a narrowing of the bistable region and a significant downward shift in the amplitude of forcing at which the saddle node bifurcations occur, and where the high branch exists. This is due to increased propagation of the forcing across the macroscale domain resulting from reduced attenuation of the oscillatory load (results not shown). For stiffer cells a lower oscillation amplitude can therefore result in the same degree of bond rupture.

Since binding affinities are specific to integrin type and can vary due to integrin activation and intracellular signalling (4, 69), we also investigate how the magnitude of and transitions between stable adhesion states respond to variations in binding affinities. In Eq. 15 the rupture rates involve parameters h_1, h_2, h_3, the ratios of unbinding rates $\hat{g}_1, \hat{g}_2, \hat{g}_3$ to the maximum binding rate $\hat{f}_1$ (see Eqs. 2, 3). Here we vary h_1, the unbinding rate for integrins at $x = 0$. We find that the magnitudes of the high stable states decrease with increased h_1 (Fig. S1(c)), since this state is obtained when adhesion formation and rupture balance, i.e. when the system is subject to only small fluctuations. Additionally, the bifurcation point on the top branch shifts to a lower value of A as h_1 increases, as deformation-induced rupture will dominate under lower loading if the bound fraction $\langle B_{tot} \rangle$ is reduced. The shift in stable branches is most notable in the upper branch since the high equilibrium bound state is more sensitive to h_1, the unbinding rate at $x = 0$, than the low oscillatory rupture
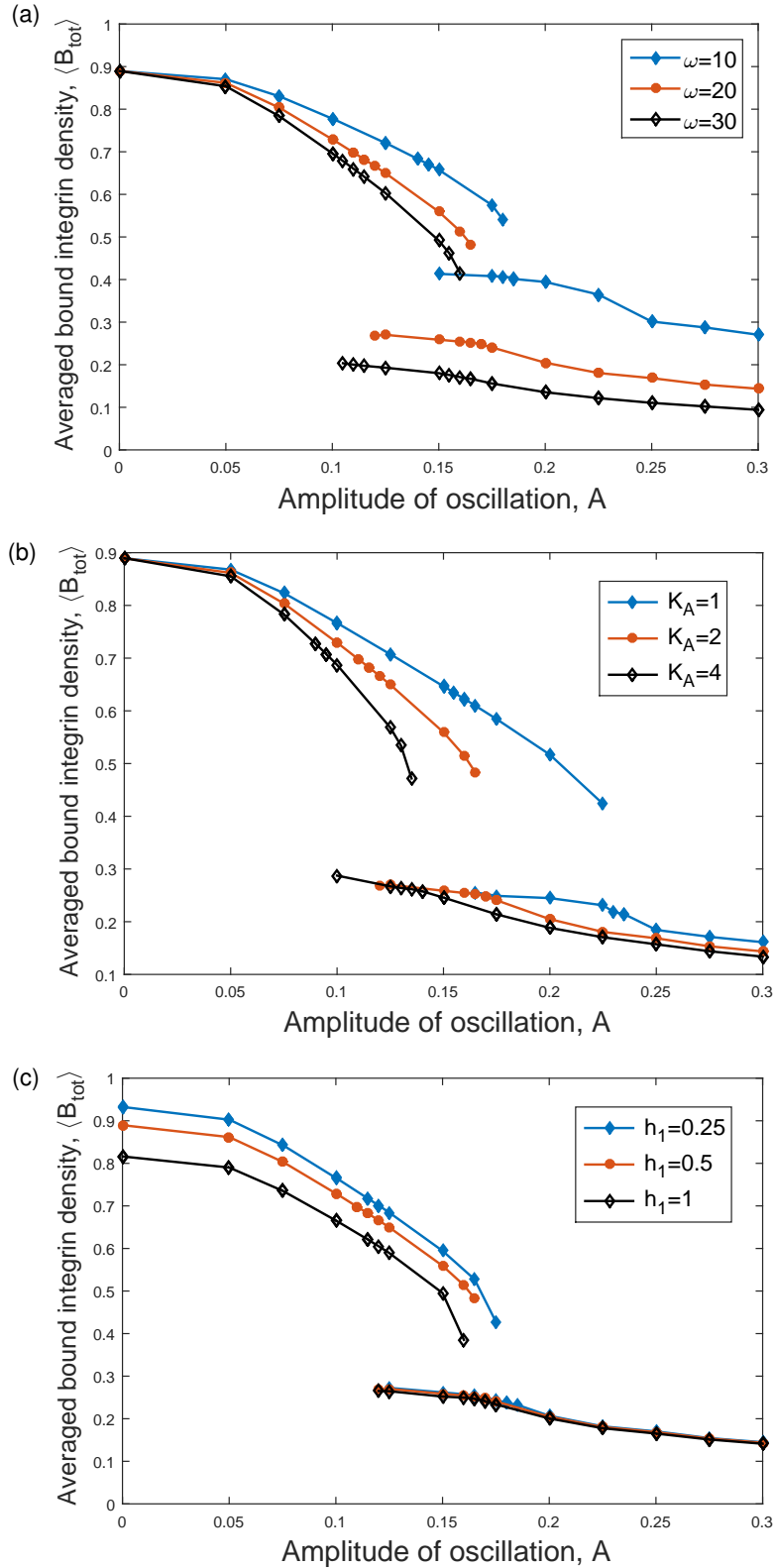
Figure S11: Stable branches in the continuum model (Section 2.2) indicating the values of $\langle B_{tot} \rangle$ (Eqs. 27,28) for: (a) varying frequencies of the oscillatory loading, $\omega = 10$, 20, and 30 (Eq. 18); (b) varying cell stiffnesses, $K_A = 1$, 2, and 4; and (c) varying integrin binding affinities $h_1 = 0.25$, 0.5 and 1 (Eq. 15). For increased frequencies, contact times for integrin binding are reduced, leading to lower averaged bound integrin densities. For increased stiffnesses, there is a significant downward shift in the amplitude of oscillation at which the saddle node bifurcations occur. Binding affinities affect the magnitude of the stable adhesion states, most notably the upper branch, as well as the position and width of the bistable region. Unless otherwise stated, dimensionless parameter values are as in Table S1.

state. In Fig. S2 we show the effect of varying h_1 with a reduced frequency of oscillatory loading, where the separation in the low branch becomes more apparent since the integrins spend more time in an unstressed state in this regime. The separation is still small since the rates h_2 and h_3, which control the unbinding of integrins in a stressed state (see Eq. 15), are dominant on this branch.
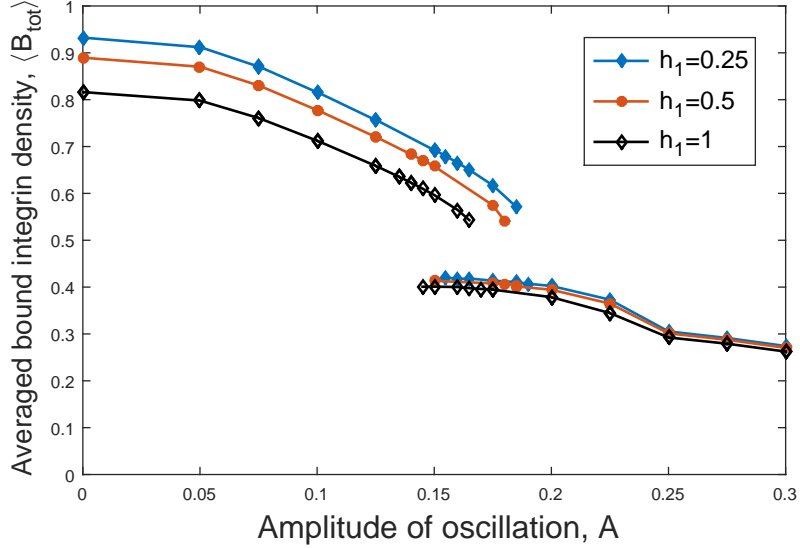

Figure S12: Stable branches indicating the values of $\langle B_{tot} \rangle$ (Eqs. 26,27) as a function of oscillation amplitude, A, for different $h_1 = 0.25, 0.5$ and 1 in Eq. 15 for $\omega = 10$. The lower branches separate (compared to in Fig. S1(c) with $\omega = 20$) due to the lower frequency of oscillations.

S.3.2 Effect of varying the input waveform

Typically, breathing is not perfectly sinusoidal, with a longer time spent on exhalation than inhalation. Here we have considered how an asymmetric waveform (accounting for physiological differences in inhalation and exhalation times) may affect the bound integrins, compared to the sinusoidal waveform used to represent breathing in the main text. We implement the asymmetry by replacing the sinusoidal displacement condition in Eq. 18 by a boundary condition of the form

$$U_E(0,t) = A\sin(\omega t + \alpha\sin(\omega t)), \tag{S4}$$

where A and ω control the amplitude and frequency of oscillation, respectively, and α is a skewness parameter. Note that Eq. 18 and the results in the main text are recovered when $\alpha = 0$. The waveform in Eq. S4 is shown in Fig. S13, where we have chosen to use $\alpha = 0.4$. Denoting the inhalation and exhalation times by t_I and t_E, respectively, this gives $t_I/t_E \approx 0.62$, which is within the range of ratios reported during tidal breathing in (68). In the sinusoidal case used in the main text (Eq. 18), this ratio was $t_I/t_E = 1$.
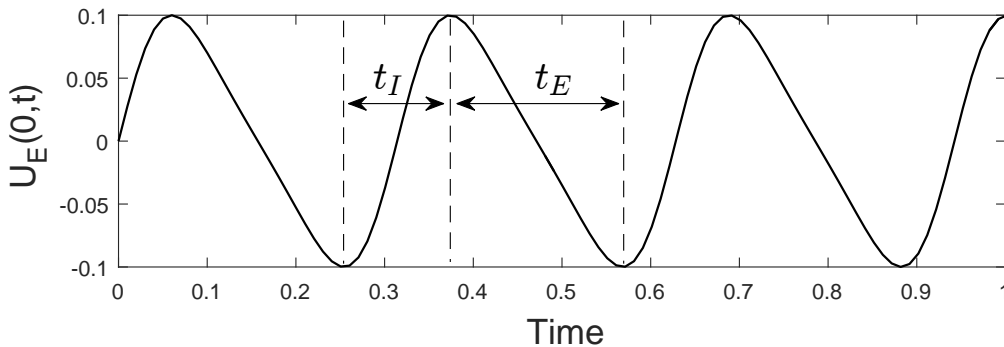

Figure S13: Plot of the asymmetric waveform used for $U_E(0,t)$, given by Eq. S4 with $\alpha = 0.4$, $A = 0.1$ and $\omega = 20$. The times t_I and t_E represent inhalation and exhalation, respectively, and in this case $t_I/t_E \approx 0.62$.

24

Since the model is driven by the relative velocity at $X = 0$ (see Eq. 23 and Section S.1.2), we differentiate Eq. S4 with respect to time to obtain

$$V(0, t) = A\omega(1 + \alpha\cos(\omega t))(\cos(\omega t + \alpha\sin(\omega t))). \tag{S5}$$

Additionally, we have used the zero displacement condition for the cell, $U_A(0, t) = 0$ (Eq. 18).

Timecourses of the total bound fraction, B_{tot}, (Eq. 27) as the oscillation amplitude, A, varies is shown in Fig. S14. For each amplitude of oscillation we consider a zero (orange) and saturated (blue) initial condition (Eq. 26), as before. Since the oscillations are now asymmetric (Fig. S13), the oscillations in the total bound fraction also exhibit asymmetry; there is more adhesion formation during the longer exhalation period, and the bound fraction therefore reaches a higher peak than during inhalation. As in Fig. 5 in the main text, for low oscillation amplitudes we find that adhesion formation dominates and a high bound integrin state is obtained. For high oscillation amplitudes, adhesion rupture dominates, resulting in a lower bound integrin regime. For intermediate oscillation amplitudes, bistability is again observed due to shared loading between integrins; the outcome depends on the initial condition.

In Fig. S15 we show the stable solution surfaces for a range of amplitudes of oscillatory loading, which corresponds to Fig. 6 in the main text. Since the results are time-averaged over a full cycle, they exhibit only slight differences. The bistable window is slightly wider (a difference of 0.05) in the asymmetric case. As the t_I/t_E value decreases from 1 (corresponding to the symmetric case), the asymmetry in the bound fraction timecourses will become increasingly apparent; however, we expect the results to exhibit the same overall dynamics.
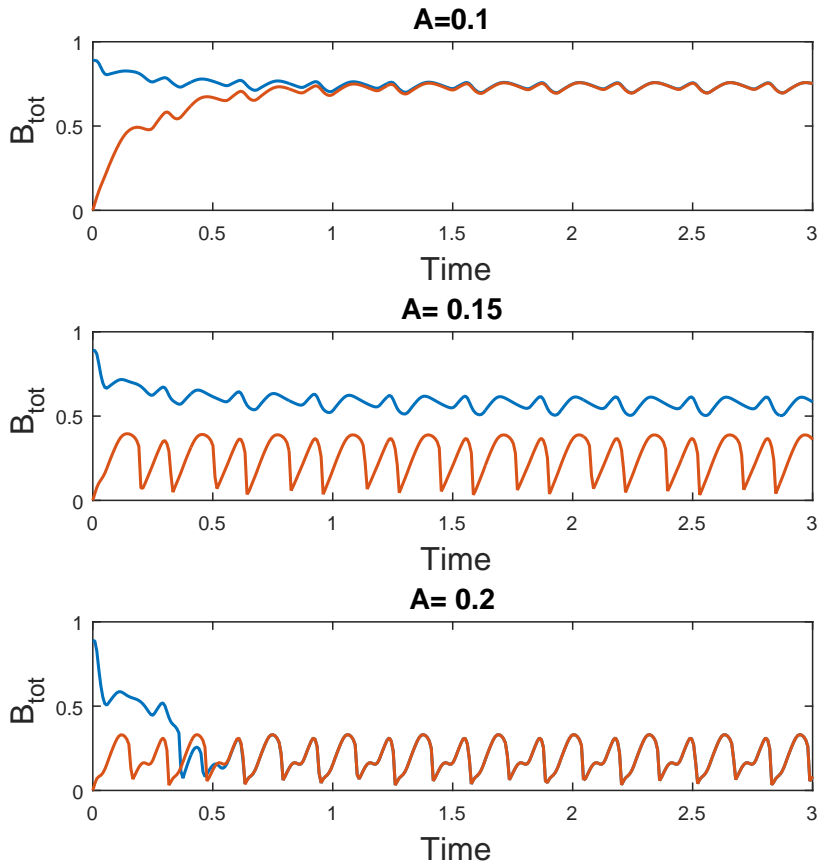

Figure S14: Timecourses illustrating the responses of total bound integrin fractions (Eq. 27) to low ($A = 0.1$), intermediate ($A = 0.15$) and high ($A = 0.2$) amplitude oscillatory loading. This is applied via the boundary conditions in Eq. S5 with $\omega = 20$. In each case we consider a zero (orange) and a saturated (blue) initial condition (Eq. 26).
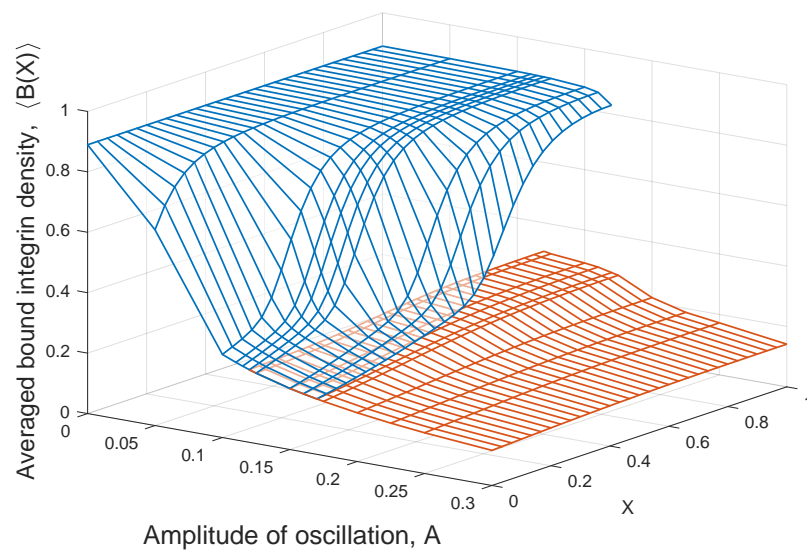
Figure S15: Upper (blue) and lower (orange) stable solution surfaces for the asymmetric waveform in Equation S4. For intermediate values of A there is bistability. The corresponding result with a symmetric waveform is shown in Fig. 6 in the main text.